electronics

MDPI

Article

An Adaptive Protection Method for Low-Voltage Distribution Networks Integrating Mechanism-Guided and Cost-Sensitive Learning

Anqi Tao [1], Zixin Li [2], Yongfu Li [1], Jinxin Ouyang [2,*], Fei Huang [1,2], Lei Xia [1], Xiping Jiang [1] and Qinglong Liao [1]

[1] Electric Power Research Institute of State Grid Chongqing Electric Power Company, Chongqing 401123, China; 15730442458@163.com (A.T.); huangfei_87@163.com (F.H.)
[2] State Key Laboratory of Power Transmission and Distribution Equipment and System Safety and New Technology, Chongqing University, Chongqing 400044, China; 20214327@stu.cqu.edu.cn
* Correspondence: jinxinoy@163.com

Abstract

In low-voltage distribution networks, load switching, induction motor start-up, photovoltaic output variations, and short-circuit faults may produce highly overlapping electrical characteristics, which can lead to maloperation or failure to operate in conventional protection. To address this problem, this paper proposes an adaptive protection method integrating physically guided and cost-sensitive learning. First, an incremental topology-constraint deviation and a voltage-current trajectory curvature are constructed based on the fault-superimposed network constraint and the variation characteristics of system equivalent impedance, enabling the discrimination of short-circuit faults from non-fault transient disturbances. Then, a cost-sensitive physically guided extreme gradient boosting (XGBoost) model is developed, in which a fault-current-increment-based weight is introduced into the objective function to enhance the learning capability for weak-fault samples. Furthermore, a temporal-consistency-based protection operation logic is designed using sliding-window confirmation and majority voting to suppress isolated abnormal predictions. Simulation and RTDS-based real-time validation results on a 0.4-kV low-voltage distribution network with distributed photovoltaic generation show that the proposed method improves weak-fault detection sensitivity and reduces maloperation under complex source–load disturbances. The method relies only on local measurements and has potential for deployment in low-voltage intelligent protection terminals.

Keywords: low-voltage distribution network; adaptive fault protection; XGBoost; physically guided weighting

Check for updates

Academic Editor: Jen-Hao Teng

Received: 24 June 2026
Revised: 17 July 2026
Accepted: 21 July 2026
Published: 22 July 2026

1. Introduction

Low-voltage distribution networks are located at the end of power systems and directly supply widely distributed end users. Owing to their relatively high line resistance-to-reactance ratios, their operating states are vulnerable to random disturbances caused by load switching and equipment start-up or shutdown [1]. Conventional overcurrent protection usually employs the current magnitude exceeding a preset threshold as the operating criterion. During the start-up of large-capacity motors or sudden load increases, inrush currents may easily cause protection maloperation. In contrast, under line-end short-circuit faults or high-impedance faults, the weak current increment may lead to protection failure to operate [2]. With the increasing penetration of distributed generation (DG) in low-voltage distribution networks, the magnitude, direction, and sequence characteristics of fault currents are altered, which weakens the applicability of conventional protection settings [3]. Regional current protection, directional overcurrent protection, and adaptive fault-current injection methods have been developed to improve protection selectivity under DG integration [4–6]. However, these protection methods still rely primarily on protection-setting coordination, directional information, or actively controlled fault-current injection. Related studies have also employed active converter control to suppress voltage fluctuations during distribution-network operation and to improve the fault-ride-through capability of grid-connected converters [7,8]. Nevertheless, these studies focus mainly on operational control and converter fault response rather than the direct discrimination of feeder short-circuit faults from non-fault transient disturbances. Therefore, existing methods do not fully address the substantial overlap between weak-fault characteristics and frequent non-fault transients in low-voltage feeders.

Existing studies on the protection of distribution networks with DG mainly focus on medium-voltage distribution networks. To address the changes in the magnitude, direction, and distribution of fault currents after DG integration, Refs. [9–11] improve conventional current protection by adjusting protection settings and constructing fault-component-based criteria. However, their performance remains dependent on setting coordination and network operating conditions. Refs. [12,13] establish pilot protection criteria using electrical quantities measured at both ends of the line, thereby reducing the influence of DG on fault-section identification. However, these methods require reliable communication channels and synchronized two-terminal measurements. For high-impedance grounding faults with small fault-current magnitudes, Refs. [14–17] construct fault detection criteria based on traveling waves, transient currents, volt-ampere characteristics, and harmonic energy, respectively. These methods provide additional transient fault information, but some of them require high sampling rates or manually tuned thresholds, and their performance may be affected by measurement noise and network parameter variations. Although these methods improve the protection performance of distribution networks with DG, they still face limitations related to threshold dependence, communication requirements, high-frequency measurements, or sensitivity to operating-condition variations. Compared with medium-voltage distribution networks, low-voltage distribution networks have relatively simplified protection configurations, more complex terminal load types, and frequent non-fault disturbances, such as motor start-up, sudden load increase, and DG output variations. In addition, line parameters and operating modes vary significantly among different distribution transformer areas. Therefore, existing methods are difficult to apply directly to reliable fault identification in low-voltage distribution networks. In contrast, the proposed method uses only local voltage and current measurements and combines physically interpretable features with cost-sensitive learning, thereby improving the discrimination between weak short-circuit faults and non-fault transient disturbances without relying on communication-assisted two-terminal information.

To reduce the influence of fixed thresholds on distribution network fault protection, machine learning methods have gradually been applied to weak-fault and high-impedance-fault detection. Ref. [18] combines wavelet denoising with random forests to achieve semi-supervised identification of high-impedance grounding faults. Ref. [19] adopts an improved extreme learning machine to construct a high-impedance grounding fault detection model. Ref. [20] combines phase-space reconstruction with transfer learning to improve model adaptability under different operating modes. Ref. [21] employs an attention mechanism and an object detection method to identify high-impedance faults. Ref. [22] improves fault classification performance through feature selection and a kernel extreme learning machine. Ref. [23] enhances the identification capability of the model for newly emerging operating conditions through incremental learning. Ref. [24] detects high-impedance faults in active distribution networks using time-frequency-spatial fused features and a hybrid convolutional neural network. These methods can establish nonlinear relationships between multidimensional electrical features and fault states. However, some of them require numerous time-domain, frequency-domain, or time-frequency-domain features, resulting in relatively complex model structures and parameter settings. Moreover, the input features are mainly obtained through data analysis, and their connection with the electrical mechanisms of faults is not sufficiently explicit.

Extreme Gradient Boosting (XGBoost) iteratively constructs multiple classification and regression trees to progressively correct prediction errors. It has the advantages of good classification performance, high training efficiency, and convenient deployment [25]. Ref. [26] reduces the false alarm rate of electricity theft detection by improving the XGBoost model. Ref. [27] employs XGBoost for measurement feature selection and combines it with a decision tree to realize distribution network topology identification. Ref. [28] uses XGBoost to directly learn the mapping relationship between zero-sequence current and high-impedance grounding faults. Ref. [29] achieves fault direction discrimination for small-current grounding faults using XGBoost and generalized feature optimization. Existing studies mainly improve model identification performance by increasing the number of input features or by improving feature selection methods. However, conventional XGBoost usually assigns the same weight to different samples during training and does not sufficiently consider the unbalanced engineering costs between failure to operate under weak faults and maloperation under non-fault disturbances. This results in insufficient identification capability for terminal-end faults and high-impedance faults. To further clarify the differences between the proposed method and recent AI-based protection methods, representative studies are compared in terms of learning algorithm, input features, required measurements, relative online computational complexity, communication requirements, and reported protection performance, as summarized in Table 1.

Table 1. Comparison of representative AI-based protection methods.

Method	Input Features and Measurements	Relative Online Computational Complexity	Communication	Reported Performance and Main Limitations
Ref. [18], Random Forest	Wavelet features; local electrical signals	Medium	No	Effective for high-impedance faults; dependent on wavelet preprocessing
Ref. [19], improved ELM	Extracted electrical features; local voltage and current	Low–medium	No	Fast identification; sensitive to feature quality and parameter settings
Ref. [20], transfer learning	Phase-space features; local electrical signals	Medium–high	No	Improved adaptability; relatively complex preprocessing
Refs. [21,24], deep learning	Image or time–frequency features; local waveforms	High	No	Strong feature extraction; relatively high computational burden
Refs. [28,29], XGBoost	Zero-sequence or transient-current features; local current	Medium	No	Good classification performance; limited physical interpretability or additional feature selection
Proposed method	Two physically interpretable features; local voltage and current	Low	No	Enhanced weak-fault sensitivity and reduced false trips using physically interpretable features

Compared with existing methods, Random-Forest-based approaches generally require additional signal preprocessing, while transfer-learning and deep-learning methods involve phase-space reconstruction, image transformation, or more complex model structures. Existing XGBoost-based methods reduce model complexity but may still rely on zero-sequence quantities or additional feature-selection procedures. In contrast, the proposed method uses only local voltage and current measurements to construct two physically interpretable features, requires no communication-assisted measurements, and avoids complex signal transformations. The cost-sensitive weighting mechanism enhances weak-fault identification, while temporal-consistency confirmation suppresses isolated false predictions. Moreover, because the cited studies use different test systems, datasets, and evaluation metrics, their reported protection performance cannot be directly compared numerically. The scientific contribution of this work lies in establishing a mechanism-to-learning protection framework that links physically derived fault characteristics, fault-severity-dependent misclassification costs, and temporal-consistency-based protection decisions within a unified protection process.

To address the above issues, this paper proposes an adaptive fault protection method for low-voltage distribution networks based on physically guided weighted XGBoost. The main contributions are as follows.

1. Two physically interpretable features, namely the incremental topology-constraint deviation and the voltage–current trajectory curvature, are formulated from local voltage and current measurements to characterize the fault-superimposed network constraint and the abrupt variation in equivalent impedance, thereby improving the discrimination between short-circuit faults and typical non-fault transient disturbances.
2. A cost-sensitive XGBoost model is developed by incorporating a fault-current-increment-based sample weighting mechanism into the training objective. This mechanism assigns higher loss penalties to weak-fault samples and consequently enhances the identification sensitivity for line-end and high-resistance faults.
3. A protection decision logic based on temporal consistency is established by combining sliding-window confirmation with majority voting. The proposed logic suppresses isolated misclassifications and improves protection security under complex source–load transient disturbances.

The remainder of this paper is organized as follows. Section 2 analyzes the characteristic differences between short-circuit faults and typical non-fault disturbances in low-voltage distribution networks, and constructs fault features for low-voltage distribution networks. Section 3 establishes the physically guided weighted XGBoost fault-identification model. Section 4 proposes the adaptive fault protection method for low-voltage distribution networks. Section 5 evaluates the proposed method through simulation case studies, uncertainty tests, computational-performance analysis, and RTDS-based real-time validation. Section 6 concludes the paper.

2. Fault Mechanism Analysis and Feature Construction for Low-Voltage Distribution Networks

Low-voltage distribution networks are located at the end of power systems and directly supply diverse terminal loads with frequent start-up and shutdown operations. Their typical topologies are mainly radial or tree-like, as shown in Figure 1, and their line resistance-to-reactance ratios are usually much higher than those of transmission networks [30]. Therefore, feeder electrical quantities are highly susceptible to random disturbances caused by load switching and equipment start-up or shutdown. Taking the start-up of a large-capacity induction motor as an example, the slip is close to 1 at the initial stage because of rotor mechanical inertia, and the motor can be regarded as a low-impedance inductive load, resulting in a sharp increase in starting inrush current [31]. Similarly, an instantaneous increase in large, concentrated loads may also cause a stepwise rise in feeder current.

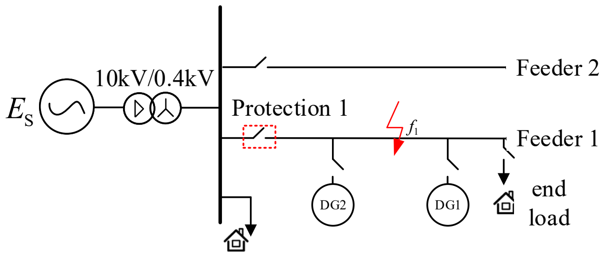

Figure 1. Topology of the low-voltage distribution network.

Overcurrent protection is commonly used in low-voltage distribution networks, with the current magnitude exceeding a preset threshold as the primary operating criterion. The threshold setting must take the maximum load disturbance into account. However, when a line-end short-circuit fault or a high-impedance fault occurs, the short-circuit path is constrained by both the impedance of the long feeder and the fault transition resistance. The current increment caused by such weak faults is often very small. It is not only much lower than that under a metallic short-circuit fault on the main feeder, but may also be close to the inrush current caused by non-fault disturbances such as motor start-up. As a result, the high current caused by strong non-fault disturbances overlaps significantly with the low fault current caused by weak faults, making it difficult for a criterion based only on current magnitude to ensure both sensitivity and reliability. Therefore, a one-dimensional current-magnitude feature is insufficient for complex operating conditions in distribution networks. It is necessary to introduce voltage-current physical constraints and transient trajectory features that reflect the intrinsic fault mechanism, so as to reliably decouple different operating conditions. The two features constructed in this paper correspond to two dominant confusion mechanisms under typical operating conditions. The incremental topology-constraint deviation determines whether the measured voltage and current increments satisfy the constraint of the fault-superimposed network and is mainly used to distinguish short-circuit faults from load changes and PV output variations. The voltage-current trajectory curvature characterizes the abrupt variation in equivalent impedance at fault inception and is mainly used to distinguish short-circuit faults from induction motor start-up, during which the equivalent impedance changes continuously because of rotor inertia. Therefore, short-circuit faults generally exhibit a relatively small incremental topology-constraint deviation and a relatively large trajectory curvature, whereas typical non-fault disturbances do not simultaneously exhibit these two characteristics. The two features are therefore complementary and enable effective discrimination between short-circuit faults and typical non-fault transient disturbances.

2.1. Incremental Topology-Constraint Deviation

When no DG is connected to the low-voltage distribution network, the equivalent network after a three-phase short-circuit fault can be decomposed, according to the superposition theorem, into the pre-fault normal-operating component network and the fault superimposed component network [10]. Since this study focuses on balanced three-phase short-circuit faults, the three-phase voltage and current quantities are symmetrical, with no negative- or zero-sequence components. Therefore, a single-phase positive-sequence equivalent network is adopted to simplify the theoretical derivation without affecting the voltage–current incremental relationship at the feeder measurement point. This representation is limited to the derivation under balanced three-phase faults and is not intended to replace a detailed three-phase model for unbalanced operation or asymmetric faults. Figure 2 shows the fault equivalent circuit without DG integration, where U_s denotes the equivalent source of the upstream system; Z_s denotes the system equivalent impedance at the source side of the outgoing feeder; Z_{load} denotes the equivalent load-side impedance at the end of the feeder; R_1 and L_1 denote the line parameters; α denotes the ratio of the distance from the transformer outlet to the fault point to the total line length; Z_f denotes the fault transition impedance.

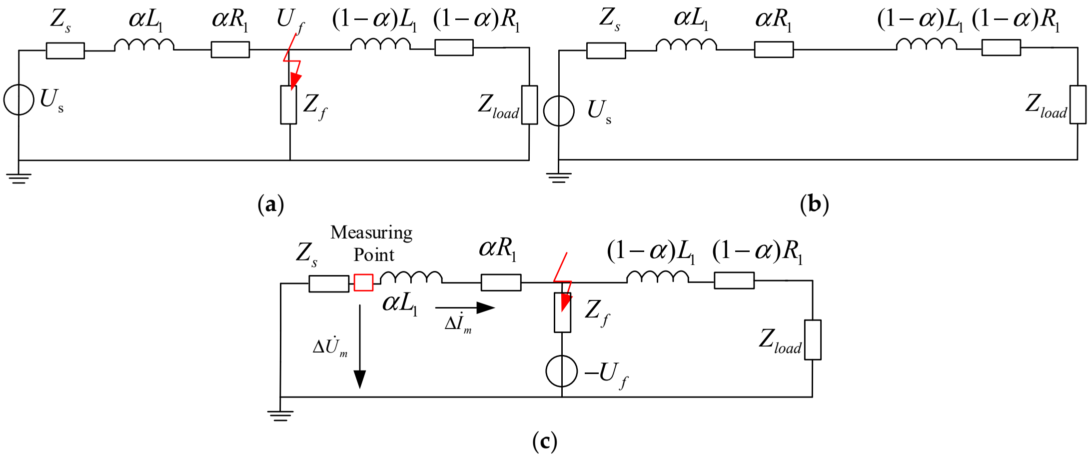

Figure 2. Fault equivalent circuit of a low-voltage distribution network without DG. (**a**) Fault equivalent circuit. (**b**) Normal-state equivalent circuit. (**c**) Fault-component equivalent circuit.

Based on Kirchhoff's voltage law, the voltage-current relationship at the outgoing feeder can be expressed as follows:

$$\dot{U}_m = \dot{U}_s - \dot{I}_m Z_s \tag{1}$$

where $\dot{I}_m$ is the outgoing feeder current phasor; $\dot{U}_m$ is the outgoing feeder voltage phasor; $\dot{U}_s$ is the equivalent voltage phasor of the upstream system.

In the fault-component network, the system source potential is set to zero, and the network is simplified into a passive network containing only impedances. When a short-circuit fault occurs, the voltage increment and current increment at the outgoing feeder satisfy the following relationship:

$$\Delta\dot{U}_{\text{m}} = -\Delta\dot{I}_{\text{m}} Z_s \tag{2}$$

where $\Delta\dot{U}_m$ and $\Delta\dot{I}_m$ are the outgoing feeder voltage-increment phasor and current-increment phasor, respectively.

When a short-circuit fault occurs in the network, the ratio of the voltage increment to the current increment is equal to the negative system equivalent impedance. When a sudden load change occurs, although the current increment is significant, the voltage increment caused by load switching is relatively small; therefore, the ratio of the voltage increment to the current increment is close to zero. Based on the above fault-component relationship, the incremental topology-constraint deviation is formulated in this paper as follows:

$$\lambda_Z = \left| \frac{\Delta\dot{U}_m}{\Delta\dot{I}_m} + Z_s \right| \tag{3}$$

where λ_Z is the incremental topology-constraint deviation.

Under a short-circuit fault, the incremental topology-constraint deviation is close to zero. In contrast, under a sudden load change, the incremental topology-constraint deviation is approximately equal to the system impedance and deviates significantly from zero. Therefore, this feature can be effectively used to distinguish short-circuit faults from sudden load changes.

When DG is connected to the line, the fault current is jointly supplied by the upstream grid and DG. The outgoing feeder current is affected by the DG's connection location and its control strategy, and the DG can be equivalent to a voltage-controlled current source [4]. According to the superposition theorem, the network is decomposed into the normal-operating component network and the fault-superimposed component network, as shown in Figure 3. Figure 3a shows the fault equivalent circuit of the low-voltage distribution network with DG, where β_1 is the ratio of the distance from the transformer outlet to the DG2 grid-connection point to the distance from the transformer outlet to the fault point, and β_2 is the ratio of the distance from the fault point to the DG1 grid-connection point to the distance from the fault point to the line end. In the fault-superimposed network shown in Figure 3c, the equivalent potential of the upstream system is set to zero, and only the system equivalent impedance Z_s is retained on the left side of the outgoing feeder. The current increment flowing through the system equivalent impedance is equal to the outgoing feeder current increment. Therefore, the ratio of the voltage increment to the current increment remains equal to the negative system equivalent impedance. After a sudden load increase, the DG output current is rapidly regulated by its control system; however, no short-circuit fault branch is formed in the system, and the voltage and current increments at the measurement point do not satisfy the constraints of the fault-superimposed network. Therefore, the incremental topology-constraint deviation under load disturbances is significantly larger than that under short-circuit faults, which can be used to distinguish short-circuit faults from load disturbances.

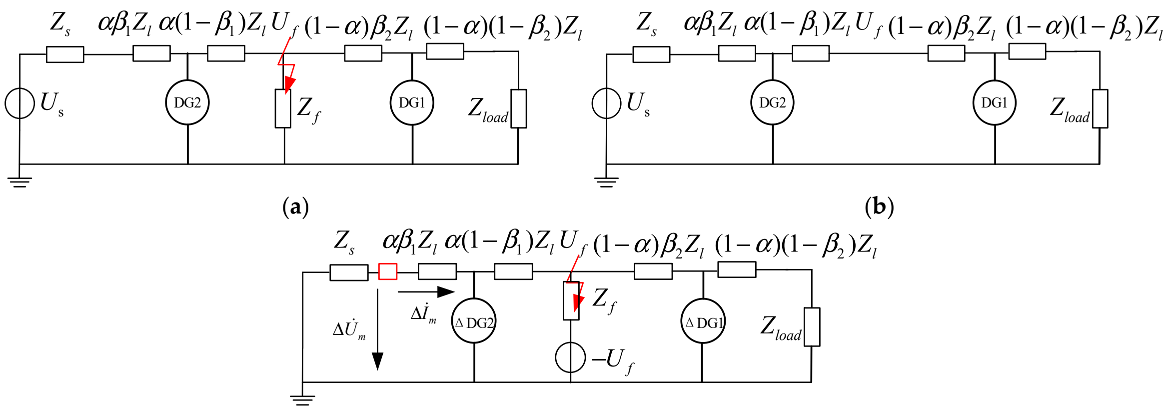

Figure 3. Fault equivalent circuit of a low-voltage distribution network with DG. (**a**) Fault equivalent circuit. (**b**) Normal-state equivalent circuit. (**c**) Fault-component equivalent circuit.

2.2. Voltage-Current Trajectory Curvature

After a three-phase short-circuit fault occurs, the line equivalent impedance changes abruptly, and the rates of change in the outgoing feeder voltage and current also undergo abrupt variations at the initial stage of the fault. As a result, the trajectory in the voltage-current phase plane exhibits an obvious corner. However, owing to rotational inertia, both the mechanical angular speed and slip vary continuously during motor start-up, and the equivalent impedance changes continuously with the slip [31]. In the voltage-current phase plane, the trajectory formed by the outgoing feeder voltage and current therefore appears as a smooth and continuous curve. Accordingly, the voltage–current trajectory curvature is introduced in this paper to distinguish short-circuit faults from induction motor start-up. For a discrete sampling sequence, the trajectory curvature at the k-th sampling point can be expressed as follows:

$$\kappa(k) = \frac{|i'(k)u''(k) - u'(k)i''(k)|}{\left[i'^2(k) + u'^2(k) + \varsigma\right]^{\frac{3}{2}}} \tag{4}$$

where $\kappa(k)$ is the trajectory curvature at the k-th sampling point; ς is a positive constant used to avoid computational errors caused by a zero denominator and to suppress noise interference; $i'(k)$ and $u'(k)$ are the first-order discrete differences in current and voltage, respectively; $i''(k)$ and $u''(k)$ are the second-order discrete differences in current and voltage, respectively, which are expressed as follows:

$$\begin{cases} i'(k) = i(k) - i(k-1) \\ u'(k) = u(k) - u(k-1) \end{cases} \tag{5}$$

$$\begin{cases} i''(k) = i(k) - 2i(k-1) + \mathrm{i}(k-2) \\ u''(k) = u(k) - 2u(k-1) + u(k-2) \end{cases} \tag{6}$$

Constrained by rotor rotational inertia, the mechanical angular speed and slip cannot change stepwise during motor start-up, and the equivalent impedance varies continuously throughout the start-up process. Therefore, the first- and second-order differences in the outgoing feeder voltage and current change relatively smoothly, resulting in a smooth voltage-current trajectory. The trajectory curvature calculated from Equations (4)–(6) varies slowly during motor start-up, generally remains at a low level, and does not produce an obvious abrupt peak. At the instant of a short-circuit fault, the fault branch is connected instantaneously, causing a step change in the system equivalent impedance and an abrupt variation in the rates of change in voltage and current at the fault inception point. i' and u' become discontinuous, while i'' and u'' exhibit large impulses. The trajectory curvature jumps at the fault instant and forms a local peak. Under the same sampling frequency, data-window length, and calculation method, the trajectory curvatures under motor start-up and short-circuit faults are shown in Figure 4.

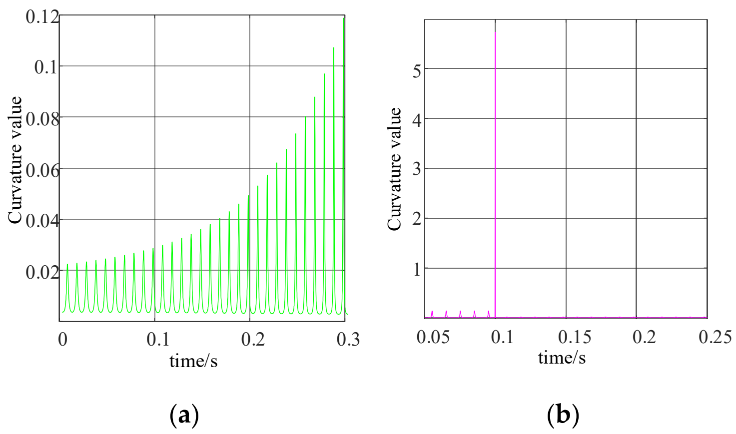

Figure 4. Trajectory curvature under motor start-up and short-circuit faults. (**a**) Motor start-up. (**b**) Short-circuit fault.

After a short-circuit fault occurs, the curvature increases rapidly and forms an obvious peak. During motor start-up, the curvature varies more smoothly, and its peak value is significantly lower. Therefore, the trajectory curvature can characterize the difference between short-circuit faults and motor start-up.

3. Physically Guided Cost-Sensitive XGBoost Identification Model

XGBoost can establish a nonlinear mapping between input features and fault states by iteratively integrating multiple classification and regression trees, and improves classification performance by fitting the prediction residuals from the previous iteration in each subsequent round. During model training, the incremental topology-constraint deviation and trajectory curvature are used as input features. Meanwhile, physically guided weights are assigned according to the current increment of fault samples, enabling the model to pay more attention to weak-fault samples during training. In the online identification stage, the model only needs to perform feature-threshold comparisons and accumulate the leaf-node weights to output the predicted probability that the current state corresponds to a short-circuit fault. The calculation process is relatively simple and has potential for deployment in low-voltage circuit breakers or edge protection terminals. The physically guided weighted XGBoost fault identification model established in this paper is shown in Figure 5.

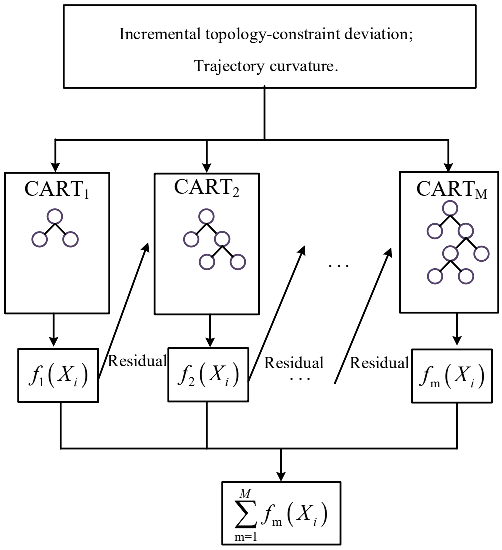

Figure 5. Fault identification model for low-voltage distribution networks.

The input feature vector of the physically guided weighted XGBoost fault identification model for low-voltage distribution networks consists of the incremental topology-constraint deviation and the trajectory curvature. Since these two features have different dimensions and numerical ranges, the min-max method is adopted to normalize the input features, so as to unify the feature scale and facilitate model input, feature comparison, and result presentation:

$$X_{ij} = \frac{x_{ij} - x_{\min,j}}{x_{\max,j} - x_{\min,j}} \tag{7}$$

where x_{ij} and X_{ij} are the values of the j-th input feature of the i-th sample before and after normalization, respectively; $x_{\min,j}$ and $x_{\max,j}$ are the minimum and maximum values of the j-th input feature, respectively; $j = 1$ denotes the incremental topology-constraint deviation, and $j = 2$ denotes the trajectory curvature.

XGBoost estimates the fault probability by integrating M classification and regression trees. During the iterative process, each base learner fits the negative gradient direction of the current objective function, and the prediction score of a sample is obtained by accumulating the leaf-node weights. The input-output relationship can be expressed as follows:

$$\hat{y}_i = \sigma\left(\sum_{m=1}^{M} f_m(X_i)\right) \tag{8}$$

where $\hat{y}_i$ is the predicted probability that the i-th sample belongs to a short-circuit fault; X_i is the input feature vector of the i-th sample; $f_m(X_i)$ is the prediction score of the m-th tree for sample X_i; σ is the Sigmoid function, which maps the prediction score to a probability in [0,1].

Based on Equation (8), the closer $\hat{y}_i$ is to 1, the higher the probability that the sample is identified as a short-circuit fault; the closer $\hat{y}_i$ is to 0, the higher the probability that the sample is identified as a non-fault disturbance. The accuracy of the predicted probability and the identification capability for boundary samples highly depend on the construction of the objective function during model training.

When calculating the loss function, conventional data-driven classification algorithms usually assume equal misclassification costs for different types of samples. However, in low-voltage distribution networks, there is a significant imbalance in engineering costs between missed detection of weak faults, namely protection failure to operate, and misclassification of non-fault disturbances, namely protection maloperation. Samples such as terminal-end weak faults have extremely small current increments and exhibit a high degree of feature overlap with normal load disturbance samples. Without differentiated treatment during model training, these high-cost weak-fault samples can be easily overwhelmed by a large amount of normal operating data, resulting in protection failure to operate. Therefore, a cost-sensitive learning mechanism is introduced in this paper. A physically guided weight based on the fault mechanism is incorporated into the training objective of XGBoost, and a cost-sensitive objective function composed of a weighted logistic loss and a tree-structure regularization term is reconstructed as follows:

$$\Gamma(\phi) = \sum_{i=1}^{N} \omega_i \cdot LogLoss(y_i, \hat{y}_i) + \sum_{m=1}^{M} \Omega(f_m) \tag{9}$$

where $\Omega(f_m)$ and $LogLoss(y_i, \hat{y}_i)$ are expressed as follows:

$$\begin{cases} \Omega(f_m) = \gamma T + \frac{1}{2}\lambda_{reg}\|\varpi\|^2 \\ LogLoss(y_i, \hat{y}_i) = y_i \ln\left(1 + e^{\hat{y}_i}\right) + (1 - y_i)\ln\left(1 + e^{\hat{y}_i}\right) \end{cases} \tag{10}$$

where $\Gamma(\phi)$ is the total loss function value of the model; N is the total number of training samples; y_i is the true label of the sample, with 1 indicating a fault and 0 indicating a non-fault condition; $\hat{y}_i$ is the predicted probability; $\Omega(f_m)$ is the regularization term used to constrain the tree structure; γ is the penalty coefficient for the number of leaf nodes and controls the tree depth; T is the total number of leaf nodes; λ_{reg} is the L_2 regularization coefficient of the weights; ϖ is the leaf-weight vector; $LogLoss(y_i, \hat{y}_i)$ is the logistic loss function; ω_i is the physically guided weight of the i-th sample:

$$\omega_\mathrm{i} = \alpha_{class} \cdot \left(1 + \beta \cdot \frac{I_{L,rat}}{\Delta I_{f.i}}\right) \tag{11}$$

where α_{class} is the class-balancing coefficient used to address the imbalance between positive and negative samples; $I_{L,rat}$ is the rated load current of the line; $\Delta I_{f.i}$ is the fault-current increment magnitude of the i-th sample; β is the physical attention factor.

The physically guided weight essentially represents the penalty cost assigned to different samples. When the fault-current increment is small, the corresponding weight increases. Such samples usually correspond to terminal-end weak faults or high-impedance faults, whose fault-current characteristics are not obvious and can be easily masked by load fluctuations. For fault samples, the physically guided weight is determined according to the magnitude of the fault-current increment. The smaller the fault-current increment, the larger the loss penalty assigned to the sample, forcing the model to strengthen the fitting of such boundary samples during the iterative training process. For non-fault disturbance samples, such as sudden load increases, motor start-up, and DG output variations, the default weight is set to 1 because their misclassification cost is relatively lower.

4. Adaptive Protection Method Based on Temporal-Consistency Confirmation

Based on the physically guided cost-sensitive XGBoost identification model, the protection device can evaluate the fault confidence of the current state with high sensitivity. However, in low-voltage distribution networks, the electrical characteristics of line-end and high-impedance faults are relatively weak, and variations in fault resistance, load level, and DG operating state may cause the transient features to exhibit certain nonlinear and stochastic characteristics. Meanwhile, frequent start-up and shutdown of large-capacity induction motors, step increases in load, and high-frequency fluctuations in DG output introduce complex transient impacts and electromagnetic background noise even under normal operating conditions. The weakness of fault features and the complexity of non-fault disturbance features are intertwined, making the single-point output of the fault identification model highly susceptible to local waveform distortion and prone to misclassification. As a result, it is difficult to cope with the complex and variable operating conditions of low-voltage distribution networks. Therefore, this paper proposes a protection operation logic that includes temporal-consistency confirmation and state-adaptive trip output.

For the starting element, to avoid the influence of load fluctuations and measurement background noise in the distribution network, an abrupt-change starting criterion based on the transient voltage-drop magnitude between adjacent sampling points is adopted:

$$U_m(\mathrm{t}+1) - U_m(\mathrm{t}) > \varepsilon_{set} \tag{12}$$

where ε_{set} is the protection starting threshold; $U_m(\mathrm{t}+1)$ and $U_m(\mathrm{t})$ are the line-voltage magnitudes at two adjacent sampling instants, respectively.

After protection starting, the measurement device collects voltage and current signals in real time and calculates the incremental topology-constraint deviation and trajectory curvature at the current sampling instant. After normalization, the feature vector is input into the trained physically guided weighted XGBoost identification model, which outputs the predicted probability $\hat{y}_{\mathrm{t}}$ that a short-circuit fault occurs in the system at the current sampling instant. In the strong-disturbance environment of low-voltage distribution networks, the single-point fault probability output by the identification model may exhibit random fluctuations. To improve the robustness of protection decisions, a sliding time-window continuous confirmation mechanism is introduced. This mechanism smooths locally abnormal confidence values by extracting the correlation characteristics of the temporal output states. Let the fault decision threshold be δ_{high} and the load decision threshold be δ_{low}. Based on the model output probabilities over the latest five consecutive sampling points, the real-time operating state of the protection device is defined as follows:

$$S(t) = \begin{cases} \text{fault state, ifCount}\left(\hat{y}_{\mathrm{t}} > \delta_{\mathrm{high}}\right) \geq 3 \\ \text{load state, ifCount}(\hat{y}_{\mathrm{t}} < \delta_{low}) \geq 3 \\ \text{latent state, otherwise} \end{cases} \tag{13}$$

where $S(t)$ is the operating state confirmed by the protection device at time t; Count denotes the number of sampling points within the latest five sampling points that satisfy the condition in parentheses.

When the fault prediction probabilities of at least three sampling points among the latest five sampling points are higher than δ_{high}, the current state is identified as a fault state. When the fault prediction probabilities of at least three sampling points among the latest five sampling points are lower than δ_{low}, the current state is identified as a load state. When neither of the two conditions is satisfied, the current state is identified as a latent state. The mechanism in Equation (13) is essentially a majority-voting logic that balances operation speed and reliability. It requires the fault features to exhibit a certain degree of temporal persistence, thereby effectively filtering out prediction anomalies caused by isolated noise spikes.

For different identified states, the protection device adopts an adaptive trip-output logic. The load state indicates that the current disturbance is most likely a non-fault condition, such as motor start-up, a sudden load increase, or DG output fluctuation. Although such conditions may cause obvious overcurrent impacts, their physical characteristics do not satisfy those of a short-circuit fault, and the predicted probability remains low. In this case, the protection device is blocked, and no trip command is issued. The latent state indicates that the predicted probabilities within the sliding window fluctuate and fail to form a high-confidence classification result. This state is commonly observed during the transient transition stage at fault inception, the unstable feature stage of high-impedance faults, or the boundary region under strong noise interference. In this case, the protection device adopts a delayed-operation strategy, maintains the original monitoring mechanism, and may issue an alarm signal according to the operating requirements of the power grid. The fault state indicates that the current disturbance has been confirmed as a short-circuit fault. Considering the combined effects of DG current sharing, DG current-limiting control, and high line impedance, the outgoing feeder fault current at this stage may be much lower than the pickup setting of conventional overcurrent protection. However, because its transient trajectory and incremental topology have exhibited significant fault characteristics and have been stably confirmed in the time dimension, the protection device can use this state as the final trip-output condition. Therefore, the protection operation criterion can be written as follows:

$$Q_{trip}(t) = \begin{cases} 1(\text{trip command}), S(t) = \text{ fault state} \\ 0(\text{protection blocking}), S(t) = \text{ load state} \\ 0(\text{protection blocking and alarm}), S(t) = \text{ latent state} \end{cases} \tag{14}$$

where $Q_{trip}(t)$ is the protection trip-output signal.

Compared with conventional overcurrent protection and standard data-driven methods, the proposed protection method shows better adaptability in both operating principle and application conditions. By incorporating a physically guided weighted XGBoost model, the proposed method mitigates the masking effect of large amounts of normal operating data on weak fault features. As a result, the identification sensitivity for weak faults is improved, and the detection capability for terminal-end faults and high-impedance faults is enhanced. In addition, the temporal-consistency confirmation mechanism suppresses single-point probability fluctuations caused by measurement noise and nonlinear transient distortion, thereby improving the reliability against maloperation and reducing the misclassification rate under complex non-fault disturbances. Furthermore, the proposed scheme uses voltage and current signals acquired by the same local protection terminal and does not rely on communication-assisted two-terminal measurements. Therefore, communication delays and inter-terminal synchronization errors do not directly enter the protection decision process.

The physically guided weighting mechanism is used only during offline training and therefore does not increase the online computational burden. From the perspective of online computation, the proposed method mainly includes the calculation and normalization of two input features, XGBoost inference, and five-point majority voting. For an XGBoost model containing M decision trees with a maximum depth of d, each inference requires no more than Md node comparisons, and its computational complexity is $O(M, d)$. The storage requirement is proportional to the total number of tree nodes, while feature normalization and majority voting introduce only constant additional computation and storage.

5. Case Study Analysis

To verify the effectiveness of the proposed protection method, a typical 0.4-kV multi-branch radial low-voltage distribution network with distributed photovoltaic generation was established in MATLAB/Simulink R2024a, as shown in Figure 6. The test system consists of a 10-kV upstream grid, a 10/0.4-kV distribution transformer, buses B1–B4, line sections L1–L5, four branch loads, two distributed photovoltaic units, and one induction motor.

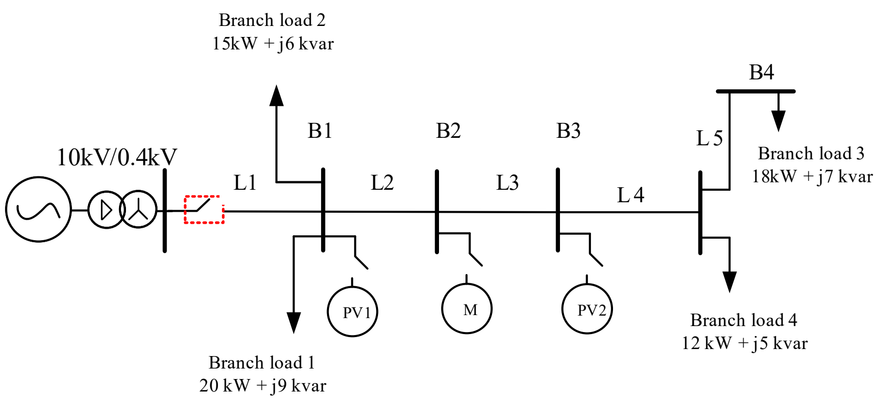

Figure 6. Simulation system.

The distribution transformer has a rated capacity of 400 kVA and a short-circuit impedance of 4%. The protection device is installed at the head end of the feeder. The total length of the protected main feeder is 1.0 km, and the positive-sequence resistance and reactance of the lines are 0.0754 Ω/km and 0.070 Ω/km, respectively.

Branch loads 1 and 2 are connected to the lateral branches around bus B1, with powers of 20 kW + j9 kvar and 15 kW + j6 kvar, respectively. Branch loads 3 and 4 are connected to the downstream branches around bus B4, with powers of 18 kW + j7 kvar and 12 kW + j5 kvar, respectively. An 18.5-kW induction motor is connected to bus B2. PV1 with a rated capacity of 30 kW is connected to bus B1, while PV2 with a rated capacity of 50 kW is connected to bus B3.

During normal operation, the photovoltaic units adopt constant-power control. During grid faults, they switch to low-voltage ride-through control, inject reactive current according to the voltage drop at the grid-connection point, and limit their output currents to 1.2 p.u.

To construct the training and testing samples for the model, a MATLAB script is used to automatically modify the simulation parameters and run the model in batches. The fault location is set within the range of 0.20–0.95 km from the head end of the feeder, and the fault resistance is set to 0.02, 0.10, 0.50, 1, 2, 5, 10, 20, 50, 100, 200, and 500 Ω, respectively, so as to cover fault characteristics under different fault locations and fault severities. The non-fault samples include sudden load increases, induction motor start-up, and PV output variations.

Specifically, the load increment is set to 10–80% of the rated load, the initial load ratio of the induction motor is set to 20–80%, and the PV output variation range is set to 10–50% of the rated capacity. Various simulation samples are automatically generated through the above parameter combinations, and the composition of different sample types is shown in Table 2. The parameter ranges in Table 2 were selected to cover fault and non-fault transient conditions with different characteristic intensities. The fault-location range extends from the upstream section to the vicinity of the feeder end, thereby considering the weakening of fault characteristics with increasing electrical distance. The fault resistance ranges from 0.02 Ω, representing a near-metallic short circuit, to 500 Ω, representing a weak high-resistance fault. The load-increment range of 10–80%, motor initial-load ratio of 20–80%, and PV output-variation range of 10–50% were selected to generate non-fault disturbances from mild variations to severe transient impacts. This parameter traversal enables the sample dataset to cover both clearly distinguishable operating conditions and boundary conditions in which fault and non-fault characteristics overlap.

Table 2. Composition of Simulation Samples.

Operating Condition	Parameter Range	Samples
Three-phase short-circuit fault	Fault location: 0.20–0.95 km; fault resistance: 0.02–500 Ω	7600
Sudden load increase	Load increment: 10–80%	2600
Motor start-up	Initial load ratio: 20–80%	2800
PV output variation	Output variation in PV1 and PV2: 10–50%	1800

All samples are stratified according to operating condition and divided into the training set and testing set at a ratio of 75% and 25%, respectively. The training set contains 11,100 samples, and the testing set contains 3700 samples. Each sample corresponds to one complete simulation scenario. After the disturbance occurs, the incremental topology-constraint deviation and trajectory curvature are calculated, and the extracted features are used for model training. Model training is completed in the offline stage. During online operation, only the trained model is invoked to output the fault prediction probability. Both simulation and model training are carried out on the MATLAB/Simulink platform. The simulations and model training were performed on a computer equipped with an AMD Ryzen 5 9600X six-core processor (Advanced Micro Devices, Inc., Santa Clara, CA, USA) with a base frequency of 3.90 GHz, 32 GB of RAM, and an NVIDIA GeForce RTX 5060 graphics card (NVIDIA Corporation, Santa Clara, CA, USA) with 8 GB of video memory.

To reduce the subjectivity in model parameter selection, five-fold cross-validation and grid search are performed on the training set to determine the number of base classifiers, the maximum tree depth, and the learning rate. The cross-validation results under different parameter combinations are shown in Figure 7. As shown in Figure 7, the cross-validation accuracy of the model under different parameter combinations is concentrated between 0.938 and 0.940, with only small overall fluctuations. This indicates that the constructed incremental topology-constraint deviation and trajectory curvature features have good stability. When the maximum tree depth is 2, the cross-validation accuracy increases from 0.938 to 0.939 as the number of base classifiers increases. When the maximum tree depth increases to 3, the accuracy under the same number of base classifiers further improves, and the highest cross-validation accuracy reaches 0.940. These results show that appropriately increasing the number of base classifiers and the tree depth can enhance the model's fitting capability for boundary samples between fault and non-fault disturbances. However, the improvement in accuracy is limited, and further increasing the model complexity does not lead to a significant improvement in identification performance. Considering both the cross-validation accuracy and the computational burden for online deployment, the parameter combination with the best cross-validation result is selected as the training parameter setting for the subsequent model.

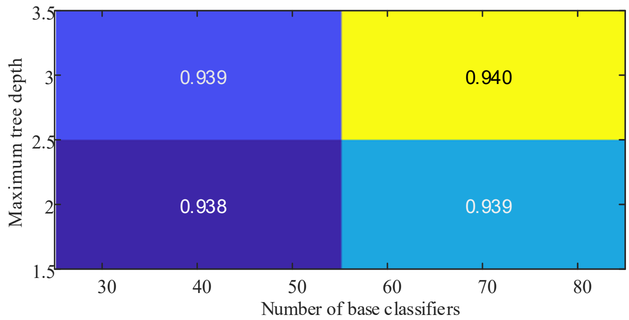

Figure 7. Cross-validation results under different parameter combinations.

Figure 8 shows the training loss variation process of the physically guided weighted XGBoost model. As shown in Figure 8, with the increase in the number of base classifiers, the weighted Logloss rapidly decreases from approximately 0.54 to approximately 0.18. Then, the decreasing rate gradually slows down, and the weighted Logloss remains basically stable at around 0.15 after 40 trees. This result indicates that the newly added classification trees can significantly correct the model prediction errors in the early training stage. As the model iteration proceeds, the error-correction effect of subsequent classification trees gradually weakens, and the model training process has basically converged. Therefore, the selected parameters can meet the requirements of subsequent fault identification.

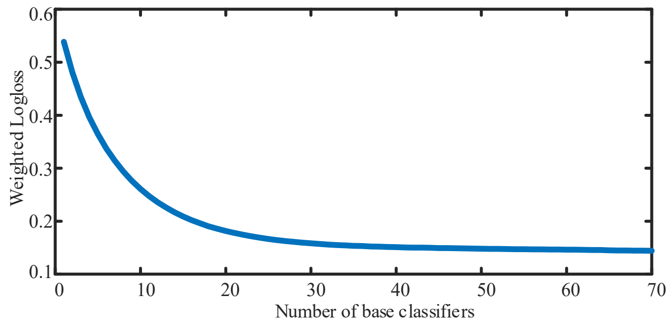

Figure 8. Training loss curve of the physically guided weighted XGBoost model.

5.1. Adaptability Verification of the Constructed Features

To verify the ability of the incremental topology-constraint deviation and trajectory curvature to distinguish three-phase short-circuit faults from typical non-fault disturbances, several operating conditions are selected for comparison, including a low-resistance three-phase short-circuit fault in the middle-to-rear section of the feeder, a terminal-end high-resistance three-phase short-circuit fault, a sudden load increase, induction motor start-up, and PV output variation. The low-resistance three-phase short-circuit fault in the middle-to-rear section is set at 0.80 km from the head end of the feeder, with a fault resistance of 0.10 Ω, representing a three-phase short-circuit condition with obvious fault characteristics. The terminal-end high-resistance three-phase short-circuit fault is set at 0.95 km from the head end of the feeder, with a fault resistance of 20 Ω, representing a weak three-phase short-circuit condition with a small current increment and a high risk of protection failure to operate. The current increment, the normalized incremental topology-constraint deviation, the normalized trajectory curvature, and the model output fault probability corresponding to each operating condition are shown in Table 3.

Table 3. Feature Values and Identification Results Under Different Operating Conditions.

Operating Condition	Current Increment/p.u.	Normalized Incremental Topology-Constraint Deviation	Normalized Trajectory Curvature	Model Output Fault Probability
Middle-to-rear-section low-resistance three-phase short-circuit fault	2.120	0.094	0.812	0.972
Terminal-end high-resistance three-phase short-circuit fault	0.240	0.318	0.427	0.884
50% sudden load increase	0.490	0.681	0.138	0.094
Direct start-up of induction motor	1.210	0.563	0.224	0.173
40% decrease in PV2 output power	0.160	0.714	0.088	0.061

As shown in Table 3, the current increment during induction motor start-up is 1.210 p.u., which is significantly higher than the current increment of 0.240 p.u. under the terminal-end weak fault. This indicates that a criterion based only on current magnitude cannot simultaneously satisfy the requirement of preventing maloperation during motor start-up and the requirement of sensitive operation under terminal-end weak faults. The normalized incremental topology-constraint deviations of the middle-to-rear-section low-resistance three-phase short-circuit fault and the terminal-end high-resistance three-phase short-circuit fault are 0.094 and 0.318, respectively, both of which are lower than those under sudden load increase, motor start-up, and PV output variation. Their normalized trajectory curvatures are 0.812 and 0.427, respectively, both of which are higher than those under non-fault disturbances. Meanwhile, the model-output fault probabilities of the two fault conditions reach 0.972 and 0.884, respectively, whereas the fault probabilities of the three non-fault disturbances are all lower than 0.20. These results indicate that the incremental topology-constraint deviation and trajectory curvature enable the model to maintain a high fault identification probability even when the weak-fault current is small, while reducing the risk of misclassification caused by strong load disturbances.

The current-increment magnitude and voltage-drop magnitude were also examined as physically meaningful candidate quantities. As demonstrated by the comparison above, the current-increment magnitude alone cannot reliably distinguish strong non-fault disturbances from weak short-circuit faults. The voltage-drop magnitude is retained only as the protection-starting quantity because it can indicate the occurrence of a transient disturbance but cannot determine whether a short-circuit branch has been formed. Therefore, it is not used as a fault-identification feature. In contrast, the incremental topology-constraint deviation and voltage–current trajectory curvature characterize the fault-superimposed network constraint and the variation pattern of equivalent impedance, respectively, thereby providing complementary physical information for fault discrimination.

5.2. Performance Comparison of Different Models

To justify the selection of the basic classifier, conventional XGBoost, Random Forest, Support Vector Machine, LogitBoost, and Bagged Trees were evaluated using the same incremental topology-constraint deviation and voltage–current trajectory curvature as input features. All classifiers used the same training and testing datasets and the same data-preprocessing procedure, and their hyperparameters were determined through five-fold cross-validation. The physically guided sample weights and temporal-consistency logic were excluded from this comparison so that only the performance of the basic classifiers was evaluated. The weak-fault detection rate and non-fault false-trip rate were selected as the evaluation metrics because they directly reflect protection failure to operate under weak faults and protection maloperation under non-fault disturbances, respectively. The comparison results are presented in Table 4.

Table 4. Performance comparison of different basic classifiers.

Algorithm	Weak-Fault Detection Rate/%	Non-Fault False-Trip Rate/%
Conventional XGBoost	88.54	4.33
Random Forest	81.95	6.11
Support Vector Machine	86.89	5.78
LogitBoost	82.58	5.78
Bagged Trees	81.89	6.00

As shown in Table 4, conventional XGBoost achieves the best overall protection performance among the five basic classifiers. Its weak-fault detection rate reaches 88.54%, which is 1.65 percentage points higher than that of the Support Vector Machine and more than 5 percentage points higher than those of Random Forest, LogitBoost, and Bagged Trees. Meanwhile, conventional XGBoost achieves the lowest non-fault false-trip rate of 4.33%. These results indicate that XGBoost provides stronger weak-fault identification capability and better security against non-fault disturbances under the same input features and dataset. Therefore, XGBoost is selected as the basic classifier of the proposed physically guided weighted model.

To further evaluate the effects of physically guided sample weighting and the sliding time-window confirmation mechanism, conventional overcurrent protection, conventional XGBoost, physically guided weighted XGBoost, and the proposed method are compared. The setting principle of conventional overcurrent protection is to avoid the maximum normal load current and the inrush current during induction motor start-up, and the pickup value is set to 1.3 times the rated current. Conventional XGBoost and physically guided weighted XGBoost use the same training set, testing set, and model parameters. The only difference lies in whether physically guided sample weights are introduced.

The testing set contains a total of 3700 simulation scenarios, including 1900 fault samples and 1800 non-fault disturbance samples. Fault samples whose fault-current increments are not greater than the rated load current of the line are defined as weak-fault samples, and the weak-fault detection rate of each method is calculated. The non-fault disturbance samples include sudden load increases, induction motor start-up, and PV output variations, and are used to evaluate the non-fault maloperation rate. Each complete simulation scenario is regarded as one test event, and the statistics are obtained according to the final state of the protection device after the disturbance occurs. The results are shown in Figure 9.

As shown in Figure 9, the weak-fault detection rate of conventional overcurrent protection is only 58.33%, while the non-fault maloperation rate reaches 9.22%. This indicates that a fixed current threshold is difficult to coordinate the sensitivity for weak faults and the reliability under strong disturbances. The weak-fault detection rate of conventional XGBoost increases to 88.54%, which is 30.21 percentage points higher than that of conventional overcurrent protection, while the non-fault maloperation rate decreases by

4.89 percentage points. This shows that the incremental topology-constraint deviation and trajectory curvature can effectively improve the discrimination capability between faults and non-fault disturbances. After physically guided sample weights are introduced, the weak-fault detection rate further increases to 96.01%, which is 7.47 percentage points higher than that of conventional XGBoost. This indicates that increasing the loss contribution of weak-fault samples can enhance the model's learning capability for weak-fault features. On this basis, after the sliding time-window confirmation mechanism is added, the weak-fault detection rate remains at 96.14%, while the non-fault maloperation rate decreases from 3.22% to 1.61%. The results demonstrate that the proposed method further reduces maloperation caused by non-fault disturbances while maintaining the detection capability for weak faults.

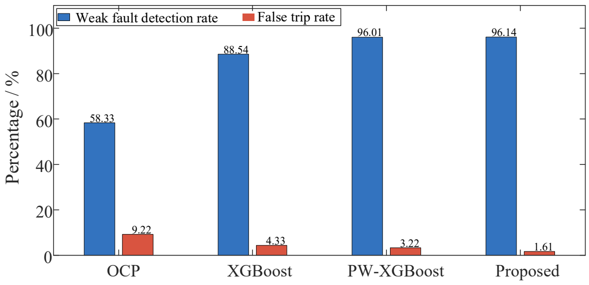

Figure 9. Performance comparison of different protection methods.

5.3. Protection Performance Under Different Fault Resistances

To further verify the sensitivity of the proposed method to weak three-phase short-circuit faults, the fault location is fixed at 0.95 km from the head end of the feeder, and the fault resistance is set to 20, 50, 100, 200, and 500 Ω, respectively. Under each fault resistance, the active output powers of PV1 and PV2 are varied, with each set to 0, 25%, 50%, 75%, and 100% of its rated capacity, to simulate weak fault characteristics under different PV output levels. Taking the fault resistance as the variable, the fault detection rates of different protection methods are calculated, and the results are shown in Figure 10.

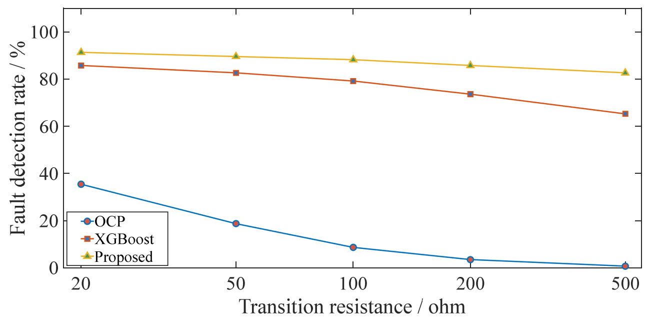

Figure 10. Line-end fault detection rates under different fault resistances.

As shown in Figure 10, as the fault resistance increases, the fault-loop impedance increases, and the fault-current increment at the head end of the feeder gradually decreases. As a result, the fault detection rates of all protection methods show a decreasing trend. Conventional overcurrent protection mainly relies on current magnitude. When the fault resistance increases from 20 Ω to 500 Ω, its fault detection rate decreases from 35.42% to 0.69%, indicating that it almost loses the ability to detect line-end high-resistance three-phase short-circuit faults. Conventional XGBoost uses the incremental topology-constraint deviation and trajectory curvature for fault identification and still achieves a detection rate of 65.28% when the fault resistance is 500 Ω. However, its detection rate decreases from 85.76% to 65.28% as the fault resistance increases, indicating that when weak fault features are further weakened, the conventional equal-weight training strategy is still insufficient for identifying boundary fault samples. The proposed method comprehensively utilizes the incremental topology-constraint deviation, trajectory curvature, physically guided cost-sensitive weighted training, and sliding time-window confirmation mechanism. Its fault detection rates reach 91.32%, 88.19%, and 82.64% when the fault resistances are 20, 100, and 500 Ω, respectively, all of which are significantly higher than those of conventional XGBoost. These results show that the proposed adaptive protection method can enhance the identification capability for line-end high-resistance three-phase short-circuit faults and improve protection sensitivity under weak fault conditions.

5.4. Protection Performance Under Different Distributed PV Operating States

To verify the adaptability of the proposed method under different PV operating states, the fault location is fixed at 0.95 km from the head end of the feeder, and the fault resistance is set to 20 Ω. According to the operating states of PV1 and PV2, the test conditions are divided into four categories: neither PV1 nor PV2 is connected; only PV1 is connected; only PV2 is connected; and both PV1 and PV2 are connected. The weak-fault detection rates of conventional XGBoost and the proposed method under different PV operating states are calculated, and the results are shown in Figure 11.

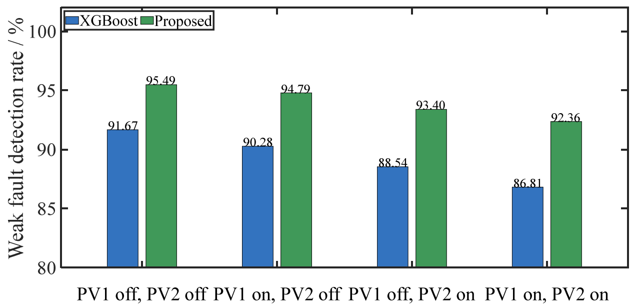

Figure 11. Weak-fault detection rates under different PV operating states.

As shown in Figure 11, as the PV operating state changes from no connection to single-point connection and then to multi-point connection, the weak-fault detection rates of both methods decrease. When neither PV1 nor PV2 is connected, the weak-fault detection rate of the proposed method is 95.49%. When only PV1 and only PV2 are connected, the detection rates are 94.79% and 93.40%, respectively. Since PV2 is located at the end of the feeder and has a larger capacity than PV1, its fault-current sharing effect has a more significant influence on the measured current at the head end of the feeder. Therefore, the detection rate when only PV2 is connected is lower than that when only PV1 is connected. When PV1 and PV2 are connected simultaneously, the detection rate of conventional XGBoost decreases to 86.81%, whereas the proposed method can still maintain a weak-fault detection rate of 92.36%. These results indicate that PV integration increases the difficulty of weak-fault identification at the head end of the feeder, but the proposed method still exhibits good adaptability under different PV operating states.

5.5. Protection Reliability Under Simultaneous Non-Fault Disturbances

To further evaluate the protection reliability under complex operating conditions, an additional independent test set containing 144 simultaneous non-fault disturbance cases was constructed. These samples were not included in the training dataset. The trained model, feature-normalization parameters, probability thresholds, and temporal-consistency logic were kept unchanged during the test.

Four types of simultaneous disturbances were considered: induction-motor start-up accompanied by a load increase; induction-motor start-up accompanied by a PV output variation; a load increase accompanied by a PV output variation; and the simultaneous occurrence of induction-motor start-up, load increase, and PV output variation. The induction-motor initial-load ratio was set to 20%, 50%, and 80%; the load-increase ratio was set to 20%, 50%, and 80%; and the PV output-variation ratio was set to 10%, 30%, and 50%. The PV variation was applied to PV1, PV2, or both units. All disturbances in each case were initiated simultaneously.

The test results are presented in Table 5. Under all 144 simultaneous-disturbance cases, the non-fault false-trip rates of conventional overcurrent protection, conventional XGBoost, physically guided weighted XGBoost, and the proposed method were 15.28%, 6.25%, 4.17%, and 2.08%, respectively. Simultaneous disturbances increased the overlap between the electrical characteristics of faults and non-fault transients. Nevertheless, the proposed method maintained the lowest overall false-trip rate because the two complementary physical features improved disturbance discrimination, while the temporal-consistency logic suppressed isolated misclassifications.

Table 5. Protection performance under simultaneous non-fault disturbances.

Simultaneous Disturbance	Number of Cases	Conventional Overcurrent Protection False-Trip Rate/%	Conventional XGBoost False-Trip Rate/%	Physically Guided Weighted XGBoost False-Trip Rate/%	Proposed Method False-Trip Rate/%
Motor start-up and load increase	9	11.11	11.11	0	0
Motor start-up and PV output variation	27	14.81	7.41	3.70	3.70
Load increase and PV output variation	27	11.11	3.70	3.70	0
Motor start-up, load increase, and PV output variation	81	17.28	6.17	4.94	2.47
Overall	144	15.28	6.25	4.17	2.08

5.6. Robustness Under Measurement and System Uncertainties

To quantitatively evaluate the robustness of the proposed method under practical measurement errors and system uncertainties, different disturbances were introduced into the original testing set. During all tests, the trained XGBoost model, feature normalization parameters, probability thresholds, and temporal consistency logic remained unchanged. According to the weak-fault definition adopted in Section 5.2, the testing set contains 1579 weak-fault cases. The weak-fault failure-to-operate rate was calculated from the number of incorrectly blocked weak-fault cases, while the non-fault maloperation rate was calculated from the final protection decisions under non-fault disturbances.

Measurement noise was simulated by adding Gaussian white noise with signal-to-noise ratios of 40, 30, 20, and 10 dB to the locally measured voltage and current signals. Local synchronization errors were represented by introducing relative mismatches of one, two, and three sampling intervals between the voltage and current channels. The corresponding results are presented in Table 6.

Table 6. Robustness under measurement noise and local voltage–current channel mismatch.

Test Condition	Disturbance Level	Weak-Fault Failure-to-Operate Rate/%	Non-Fault Maloperation Rate/%
Original testing set	None	3.86	1.61
Gaussian white noise	40 dB	4.05	1.72
Gaussian white noise	30 dB	4.43	1.89
Gaussian white noise	20 dB	5.19	2.22
Gaussian white noise	10 dB	6.59	3.06
V–I channel mismatch	1 sampling interval	4.31	1.78
V–I channel mismatch	2 sampling intervals	4.88	2.06
V–I channel mismatch	3 sampling intervals	5.32	2.44

As shown in Table 6, decreasing the signal-to-noise ratio from 40 to 10 dB increases the weak-fault failure-to-operate rate from 4.05% to 6.59% and the non-fault maloperation rate from 1.72% to 3.06%. Measurement noise directly affects the voltage and current increments and is further amplified during the difference and curvature calculations. Consequently, the incremental topology-constraint deviation and voltage–current trajectory curvature exhibit increasing fluctuations as the noise level increases.

When the voltage–current channel mismatch increases from one to three sampling intervals, the weak-fault failure-to-operate rate increases from 4.31% to 5.32%, while the non-fault maloperation rate increases from 1.78% to 2.44%. The channel mismatch changes the temporal correspondence between the voltage and current samples and consequently affects the calculation of both physical features. Nevertheless, the deterioration remains limited under the considered mismatch levels. The proposed method uses voltage and current signals acquired by the same local protection terminal and does not require remote-end measurements or communication-assisted protection information. Therefore, communication delays and inter-terminal synchronization errors do not directly enter the protection decision process. The voltage–current channel-mismatch tests specifically evaluate the influence of synchronization errors between local measurement channels.

Current-transformer inaccuracies were simulated by introducing ratio errors of ±1%, ±3%, and ±5% into the measured current. Line-parameter uncertainties were evaluated by introducing simultaneous deviations of ±5%, ±10%, and ±15% into the line resistance and reactance used for calculating the incremental topology-constraint deviation. The corresponding results are presented in Table 7.

Table 7. Robustness under current-transformer inaccuracies and line-parameter uncertainties.

Test Condition	Disturbance Level	Weak-Fault Failure-to-Operate Rate/%	Non-Fault Maloperation Rate/%
Current-transformer ratio error	±1%	3.99	1.67
Current-transformer ratio error	±3%	4.31	1.83
Current-transformer ratio error	±5%	4.75	2.06
Line-parameter deviation	±5%	4.24	1.78
Line-parameter deviation	±10%	4.69	2.06
Line-parameter deviation	±15%	5.19	2.33

As shown in Table 7, current-transformer ratio errors have a relatively limited influence on protection performance. When the ratio error increases from ±1% to ±5%, the weak-fault failure-to-operate rate increases from 3.99% to 4.75%, while the non-fault maloperation rate increases from 1.67% to 2.06%. The ratio error mainly changes the magnitude scale of the measured current. Because the proposed method does not use current magnitude as the sole protection criterion, the complementary physical features reduce the influence of this error.

Line-parameter deviations directly affect the system equivalent impedance used to calculate the incremental topology-constraint deviation. When the parameter deviation reaches $\pm$ 15%, the weak-fault failure-to-operate rate increases to 5.19%, and the non-fault maloperation rate increases to 2.33%. However, the voltage–current trajectory curvature does not directly depend on the line parameters. Therefore, the complementary use of the two features limits the deterioration caused by parameter uncertainties.

Topology changes were established based on the complete multi-branch radial network shown in Figure 6 by changing the connection states of different lateral loads. Five representative topology conditions were considered. In addition, a combined measurement-uncertainty condition and a combined measurement–parameter–topology uncertainty condition were established. The combined measurement condition included 30 dB Gaussian white noise, a one-sampling-interval voltage–current mismatch, and a $\pm$3% current-transformer ratio error. The combined uncertainty condition further included a $\pm$10% line-parameter deviation and simultaneous disconnection of Branch loads 2 and 4. The corresponding results are presented in Table 8.

Table 8. Robustness under topology changes and combined uncertainties.

Test Condition	Disturbance Level	Weak-Fault Failure-to-Operate Rate/%	Non-Fault Maloperation Rate/%
Topology change	Branch load 1 disconnected	4.94	2.11
Topology change	Branch load 2 disconnected	5.19	2.17
Topology change	Branch load 3 disconnected	4.81	2.06
Topology change	Branch load 4 disconnected	5.07	2.28
Multiple topology changes	Branch loads 2 and 4 disconnected	5.45	2.39
Combined measurement uncertainty	30 dB noise + 1-sample mismatch + $\pm$3% CT ratio error	5.13	2.28
Combined uncertainty	Measurement uncertainty + $\pm$10% parameter deviation + topology changes	7.22	3.33

As shown in Table 8, different lateral-branch changes have different effects on protection performance because the locations and powers of the disconnected loads result in different changes in feeder voltage, current, and equivalent impedance. Disconnecting Branch loads 2 and 4 simultaneously produces the greatest influence among the topology-change conditions, with a weak-fault failure-to-operate rate of 5.45% and a non-fault maloperation rate of 2.39%.

Under the combined measurement-uncertainty condition, the weak-fault failure-to-operate rate is 5.13%, and the non-fault maloperation rate is 2.28%. When measurement errors, a $\pm$10% line-parameter deviation, and topology changes are applied simultaneously, the corresponding rates increase to 7.22% and 3.33%, respectively. Under this condition, 1465 of the 1579 weak-fault cases are correctly detected, corresponding to a weak-fault detection rate of 92.78%. Although multiple uncertainties produce more evident performance degradation than individual disturbances, the proposed method still operates correctly for more than 92% of weak-fault cases and remains blocked for more than 96% of non-fault cases. These results demonstrate that the proposed method retains effective discrimination between weak short-circuit faults and non-fault transient disturbances under the considered measurement and system uncertainties.

https://doi.org/10.3390/electronics15143239

5.7. Computational Burden and Real-Time Implementation Capability

To quantitatively evaluate the online computational burden, the trained XGBoost model was tested using a CPU-based MATLAB implementation on a computer equipped with an AMD Ryzen 5 9600X six-core processor with a base frequency of 3.90 GHz and 32 GB of RAM. Before formal timing, the prediction procedure was executed once to reduce the effects of model initialization and cache loading. The complete testing set was then predicted repeatedly 20 times, and the accumulated execution time was converted into the average single-sample inference time.

The final classifier contains 70 decision trees with a maximum depth of 3. The quantitative results are listed in Table 9. The measured single-sample inference time is 1.398 μs, and the serialized model occupies 34.385 kB in MATLAB MAT-file format. The inference-stage processor-time occupancy was calculated as the ratio of the measured single-sample inference time to the selected online execution interval. Based on the measured inference time, the classifier occupies approximately 1.40% of the computation-time budget when the online execution interval is 0.1 ms and approximately 0.14% when the execution interval is 1 ms.

Table 9. Computational performance of the proposed protection method.

Performance Index	Result
Number of decision trees	70
Maximum tree depth	3
Maximum node comparisons per inference	210
Single-sample XGBoost inference time/μs	1.398
Trained-model storage/kB	34.385
Inference-stage processor-time occupancy at a 0.1-ms interval/%	1.40
Inference-stage processor-time occupancy at a 1-ms interval/%	0.14

The measured execution time corresponds to the XGBoost inference stage. The feature-calculation and temporal-consistency procedures involve fixed-order calculations and fixed-length logical operations, as described in Section 4, and their computational burden does not increase with the number of training samples. The results indicate that the XGBoost inference stage has limited execution-time and model-storage requirements on the adopted CPU platform, providing quantitative evidence of the implementation potential of the proposed method in low-voltage intelligent protection terminals.

5.8. RTDS-Based Real-Time Validation

To evaluate the protection performance of the proposed method using independently generated real-time simulation data, an RTDS-based validation system was established. The main circuit of the low-voltage distribution network, including the distributed photovoltaic units, loads, and induction motor, was implemented in Rack 1. The physical-feature calculation, XGBoost inference, temporal-consistency confirmation, and trip-output logic were implemented in Rack 2. Communication between the two racks was used to establish the complete real-time protection validation system.

The XGBoost model was trained offline using the MATLAB/Simulink dataset described in the previous subsections. After training, the tree structures, leaf weights, feature-normalization parameters, probability thresholds, and temporal-consistency parameters were fixed and directly deployed in the RTDS protection module. The RTDS-generated data were used only for independent testing, and no model retraining or parameter adjustment was performed during the RTDS tests.

A total of 180 RTDS test cases were established, including 90 fault cases and 90 non-fault disturbance cases. The fault cases consisted of middle-to-rear-section low-resistance faults, terminal-end faults with a fault resistance of 4 Ω, and terminal-end weak faults with a fault resistance of 500 Ω, with 30 cases for each condition. The non-fault cases consisted of sudden load increases, induction-motor start-up, and photovoltaic output variations, also with 30 cases for each condition. Different fault inception angles, pre-fault load levels, photovoltaic output levels, and disturbance magnitudes were considered in the tests.

For each test case, the voltage and current measurements generated by RTDS were processed through the complete online protection procedure, including physical-feature calculation, XGBoost inference, temporal-consistency confirmation, and trip-output generation. The fault operation rate was calculated as the ratio of correctly tripped fault cases to the total number of fault cases. The non-fault false-trip rate was calculated as the ratio of incorrectly tripped non-fault cases to the total number of non-fault cases. The corresponding results are summarized in Table 10.

Table 10. RTDS-based real-time validation results of the proposed protection method.

Operating Condition	Number of Cases	Fault Operation Rate/%	Non-Fault False-Trip Rate/%	Mean Operation Time/ms
Middle-to-rear-section low-resistance	30	100.00	—	11.80
Terminal-end fault, $R_f = 4\ \Omega$	30	93.33	—	14.60
Terminal-end fault, $R_f = 500\ \Omega$	30	83.33	—	18.90
Sudden load increase	30	—	3.33	—
Induction-motor start-up	30	—	3.33	—
Photovoltaic output variation	30	—	0	—
Overall	180	92.22	2.22	—

As shown in Table 10, the fault operation rates under the middle-to-rear-section low-resistance fault, terminal-end 4 Ω fault, and terminal-end 500 Ω fault conditions were 100.00%, 93.33%, and 83.33%, respectively. The non-fault false-trip rates under sudden load increases, induction-motor start-up, and photovoltaic output variations were 3.33%, 3.33%, and 0%, respectively. The mean operation times for the three fault conditions were 11.80 ms, 14.60 ms, and 18.90 ms, respectively. The overall fault operation rate was 92.22%, while the overall non-fault false-trip rate was 2.22%. These results indicate that the fixed protection model can effectively distinguish independently generated RTDS fault data from non-fault transient disturbances.

Figure 12 presents representative RTDS-based real-time protection results for a terminal-end three-phase short-circuit fault with a fault resistance of 4 Ω and an induction-motor start-up condition. After the terminal-end fault occurs, the fault probability rises above and remains above the threshold of 0.70, and the trip signal is issued after temporal-consistency confirmation. During induction-motor start-up, the fault probability increases briefly but remains below the threshold, and the protection remains blocked.

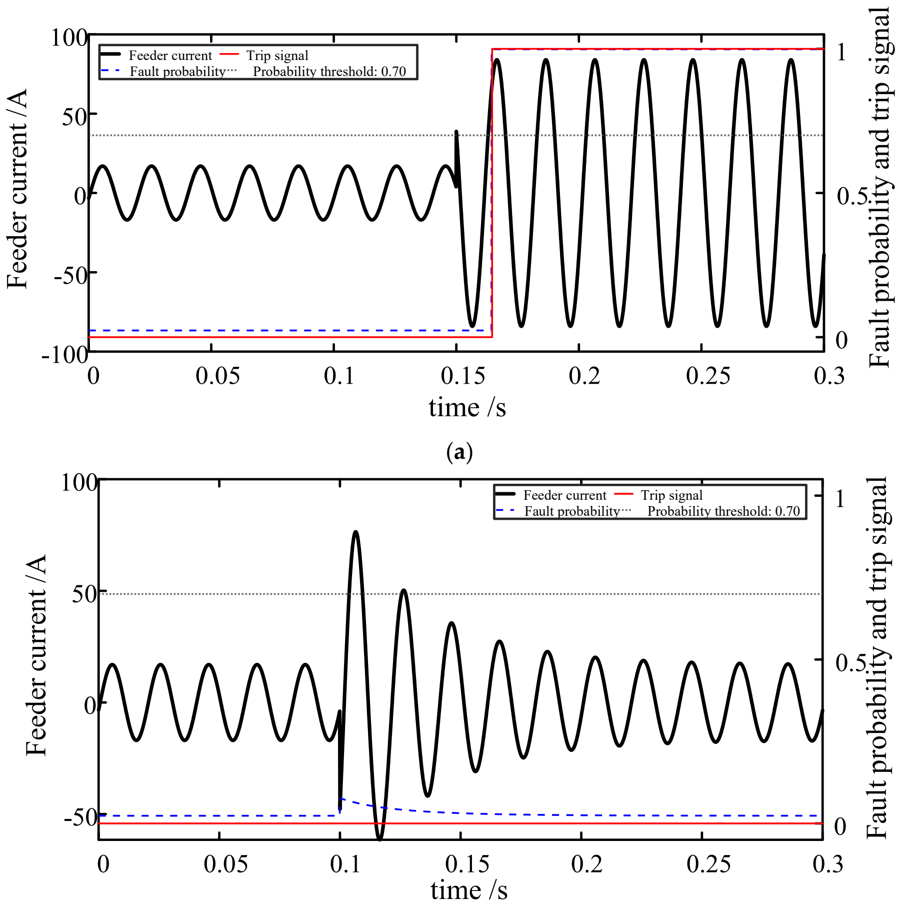

Figure 12. Representative RTDS-based real-time protection results. (**a**) Terminal-end high-resistance fault with $R_f = 4\Omega$. (**b**) Induction-motor start-up.

6. Conclusions

This paper proposes an adaptive protection method that integrates a physically guided weighted XGBoost classifier with temporal-consistency confirmation for fault identification in low-voltage distribution networks containing DG and complex source–load disturbances. First, the incremental topology-constraint deviation and the transient voltage–current trajectory curvature are constructed to characterize the differences in fault-superimposed network constraints and variations in system equivalent impedance under different operating conditions. These features enable effective discrimination between short-circuit faults and non-fault transient disturbances, including load switching, induction-motor start-up, and photovoltaic-output variations. Second, a cost-sensitive physically guided XGBoost model is developed to address the unequal engineering costs of different misclassifications. The current-increment magnitude, which reflects fault severity, is converted into a physically guided sample weight and incorporated into the objective function, thereby increasing the penalty assigned to weak-fault misclassification during iterative training. Furthermore, a temporal-consistency-based protection logic combining sliding-window confirmation and majority voting is designed to suppress isolated prediction anomalies and reduce maloperations under complex source–load disturbances.

In the test system, the proposed method achieved a weak-fault detection rate of 96.14% and a non-fault maloperation rate of 1.61%. The detection rate was 82.64% for line-end three-phase short-circuit faults with a fault resistance of 500 Ω and 92.36% when both distributed PV units were connected. Under the combined uncertainty condition involving measurement errors, line-parameter deviations, and topology changes, the weak-fault detection rate remained 92.78%, while the non-fault maloperation rate was 3.33%. These results demonstrate that the proposed method retains effective fault-discrimination capability under weak-fault conditions, different PV operating states, and representative practical uncertainties. Furthermore, the RTDS-based real-time tests achieved an overall fault operation rate of 92.22% and an overall non-fault false-trip rate of 2.22%, with mean operation times ranging from 11.80 ms to 18.90 ms under the considered fault conditions.

The proposed protection method relies only on local voltage and current measurements and does not require communication-assisted two-terminal information, indicating its potential for implementation in intelligent low-voltage protection terminals. Quantitative computational tests show that the final XGBoost classifier, containing 70 decision trees with a maximum depth of 3, requires an average single-sample inference time of 1.398 µs and a serialized model storage of 34.385 kB. The inference-stage processor-time occupancy is approximately 1.40% and 0.14% for online execution intervals of 0.1 ms and 1 ms, respectively. These results provide quantitative evidence of the low inference burden and implementation potential of the proposed method in intelligent low-voltage protection relays. The feature-construction framework is also applicable to wind-integrated distribution networks because it is determined by fault-superimposed network constraints and variations in system equivalent impedance rather than by the DG type. In practical applications, however, the transient effects of wind-turbine fault-ride-through control, current limiting, and control-mode switching should be considered. The present study was validated on a typical multi-branch radial low-voltage distribution network under both independent and simultaneous non-fault disturbances. For asymmetric faults, the incremental topology-constraint deviation and voltage–current trajectory curvature will be reconstructed using phase-domain or sequence-component quantities, and the model will be retrained using the corresponding fault samples. Future work will also address different DG penetration levels, hybrid integration of multiple DG types, larger dynamically reconfigurable network topologies, more diverse combinations of simultaneous disturbances, and broader source–load operating conditions.

Author Contributions: Conceptualization, Z.L. and J.O.; methodology, J.O.; software, A.T.; validation, Z.L. and J.O.; formal analysis, Y.L.; investigation, F.H.; resources, Z.L. and J.O.; data curation, Z.L.; writing—original draft preparation, X.J.; writing—review and editing, A.T., Y.L., J.O., F.H., L.X., X.J. and Q.L.; visualization, Z.L.; supervision, J.O. and A.T.; project administration, J.O.; funding acquisition, J.O. All authors have read and agreed to the published version of the manuscript.

Funding: This research was supported by the Science and Technology Project of State Grid Corporation of China, Project No. 52202325000W.

Institutional Review Board Statement: Not applicable.

Informed Consent Statement: Not applicable.

Data Availability Statement: The datasets presented in this article are not publicly available because they are part of an ongoing study. The datasets are available from the corresponding author upon reasonable request. Requests to access the datasets should be directed to Jinxin Ouyang (jinxinoy@163.com).

Conflicts of Interest: Authors A.T., Y.L., F.H., L.X., X.J. and Q.L. were employed by the Electric Power Research Institute of State Grid Chongqing Electric Power Company. The authors declare that this study received funding from the Science and Technology Project of State Grid Corporation of China, Project No. 52202325000W, Contract No. SGCQDK00PDJS2500132. The funder had no involvement in the study design; in the collection, analyses, or interpretation of data; in the writing of the manuscript; or in the decision to publish the results. The remaining authors declare that the research was conducted in the absence of any commercial or financial relationships that could be construed as a potential conflict of interest.

References

1. Cao, Y.; Tang, J.; Shi, S.; Cai, D.; Zhang, L.; Xiong, P. Fault Diagnosis Techniques for Electrical Distribution Network Based on Artificial Intelligence and Signal Processing: A Review. *Processes* **2025**, *13*, 48.
2. Miao, X.; Zhao, D.; Liu, X.; Hong, C.; Zhuang, S. Review on Short-Circuit Protection of Distribution Networks with Distributed Generation. *High Volt. Eng.* **2023**, *49*, 3006–3019.
3. Haddadi, A.; Farantatos, E.; Kocar, I.; Karaagac, U. Impact of Inverter-Based Resources on System Protection. *Energies* **2021**, *14*, 1050. [CrossRef]
4. Qiao, Y.; Wu, H.; Wu, T.; Li, X. Regional Current Protection for Distribution Networks with Inverter-Interfaced Distributed Generation. *Trans. China Electrotech. Soc.* **2022**, *37*, 134–144.
5. Gómez-Luna, E.; De La Cruz, J.; Vasquez, J.C. New Approach for Validation of a Directional Overcurrent Protection Scheme in a Ring Distribution Network with Integration of Distributed Energy Resources Using Digital Twins. *Energies* **2024**, *17*, 1677. [CrossRef]
6. Xu, S.; Pan, X.; Li, S.; Ouyang, J.; Zhang, L.; Ding, Z. Single-Phase Grounding Fault Protection Method for Distribution Networks Based on Photovoltaic Adaptive Injection Amount. *Power Syst. Clean Energy* **2023**, *39*, 140–150.
7. Ouyang, J.; Chen, J.; Yuan, Y.; Xu, S. Suppression Method for Voltage Fluctuation During Distribution Network Loop Closing Based on Active Control of Distributed Generation. *Electr. Power Autom. Equip.* **2024**, *44*, 49–56.
8. Chen, J.; Ouyang, J.; Huang, F.; Huangfu, B. Modelling of AC–DC Voltage Control Coupling and Adaptive Fault Ride-Through Method for VSC-HVDC Integrated Wind Farms. *IEEE Trans. Sustain. Energy* **2025**, *16*, 2533–2546. [CrossRef]
9. Xie, M.; Wang, T.; Xu, J.; Shao, Q.; Yu, Y.; Zhang, W. Influence of Distributed Generation on Distribution Network Relay Protection and Comprehensive Improved Protection Scheme. *Power Syst. Prot. Control* **2019**, *47*, 78–84.
10. Chen, X.; Li, Y.; Tan, H.; Zhao, M.; Wen, A.; Liu, N. Adaptive Positive-Sequence Current Instantaneous Protection for Distribution Networks with Inverter-Interfaced Distributed Generation. *Autom. Electr. Power Syst.* **2015**, *39*, 107–112.
11. Ma, J.; Wang, X.; Mi, C.; Wang, Z. A New Adaptive Protection Method for Distribution Networks with Distributed Generation. *Power Syst. Technol.* **2011**, *35*, 204–208.
12. Zhu, G.; Lu, Y. Study on Pilot Protection Scheme for Distribution Networks with DG. *Proc. CSEE* **2012**, *32*, 134–141.
13. Cong, W.; Pan, Z.; Wang, C.; Yu, C.; Wang, W.; Xun, T.; Song, Z. Area Pilot Protection Scheme for Distribution Systems with High Penetration of DG. *Autom. Electr. Power Syst.* **2009**, *33*, 81–85.
14. Xiao, M.; Zeng, J.; Zhou, Z.; Zhang, Q.; Deng, L.; Peng, F. High Impedance Fault Line Detection Based on Current Traveling Wave Spectrum Symmetry Driving for New Distribution Network. *Symmetry* **2025**, *17*, 775. [CrossRef]
15. Xue, Y.; Li, J.; Chen, X.; Xu, B.; Li, T. Transient Fault Line Selection and Transition Resistance Identification for High-Resistance Grounding Faults in Resonant Grounding Systems. *Proc. CSEE* **2017**, *37*, 5037–5048.
16. Wang, B.; Geng, J.; Dong, X. Analysis and Detection of Volt-Ampere Characteristics of High-Impedance Grounding Faults in Distribution Networks. *Proc. CSEE* **2014**, *34*, 3815–3823.
17. Wei, M.; Zhang, H.; Shi, F.; Xie, W.; Zhang, Y.; Fang, C. Identification of Arc Grounding Faults in Distribution Networks Based on Harmonic Energy and Waveform Distortion. *Autom. Electr. Power Syst.* **2019**, *43*, 148–154.
18. Bai, H.; Pan, S.; Shao, X.; Gao, J.; Li, W.; Lei, J.; Guo, M. Semi-Supervised Identification Method for High-Impedance Grounding Faults in Distribution Networks Based on Wavelet Denoising and Random Forest. *Power Syst. Prot. Control* **2022**, *50*, 79–87.
19. Liu, K.; Zhan, H.; Tan, Y.; Ke, L.; Li, B.; Liao, K. Detection Scheme for High-Impedance Grounding Faults in Distribution Networks Based on Improved Extreme Learning Machine. *Power Syst. Technol.* **2023**, *47*, 1886–1899.
20. Yang, G.; Wang, K.; Gao, W. High-Impedance Grounding Fault Detection in Distribution Networks Based on Phase-Space Reconstruction and Transfer Learning. *Power Syst. Prot. Control* **2022**, *50*, 151–162.
21. Zhang, Y.; Wang, X.; Luo, Y.; Zhang, D.; Mirsaeidi, S.; He, J. High Impedance Fault Detection Based on Attention Mechanism and Object Identification. *CSEE J. Power Energy Syst.* **2024**, *10*, 197–207.
22. Sheng, W.; Liu, K.; Jia, D.; Wang, Y. An Improved High-Impedance Fault Identification Scheme for Distribution Networks Based on Kernel Extreme Learning Machine. *Int. J. Electr. Power Energy Syst.* **2024**, *155*, 109543. [CrossRef]
23. Bai, H.; Gao, J.; Liu, T.; Guo, Z.-Y.; Guo, M.-F. Explainable Incremental Learning for High-Impedance Fault Detection in Distribution Networks. *Comput. Electr. Eng.* **2025**, *122*, 110006. [CrossRef]
24. Wang, C.; Feng, L.; Hou, S.; Ren, G.; Lu, T. A High-Impedance Fault Detection Method for Active Distribution Networks Based on Time–Frequency–Space Domain Fusion Features and Hybrid Convolutional Neural Network. *Processes* **2024**, *12*, 2712. [CrossRef]
25. Chen, T.; Guestrin, C. XGBoost: A Scalable Tree Boosting System. In *Proceedings of the 22nd ACM SIGKDD International Conference on Knowledge Discovery and Data Mining, San Francisco, CA, USA, 13–17 August 2016*; ACM: New York, NY, USA, 2016; pp. 785–794.
26. Chen, G.; Li, D.; Chen, X. Detection Method of Electricity Theft with Low False Alarm Rate Based on an Improved XGBoost Model. *Power Syst. Prot. Control* **2021**, *49*, 178–186.
27. Zhang, L.; Wang, J.; Xu, S.; Zhang, M.; Li, B.; Tang, Y. Distribution Network Topology Identification Method Based on XGBoost Feature Selection and Decision Tree Multi-Label Classification. *Power Syst. Clean Energy* **2025**, *41*, 10–21.

https://doi.org/10.3390/electronics15143239

28. Ke, L.; Li, B.; Liao, K.; Tan, Y.; Jia, Y.; Duan, Q.; Sha, G. High-Impedance Fault Detection Method in a Distribution Network Based on XGBoost. *Power Syst. Prot. Control* **2024**, *52*, 88–98.
29. Wang, J.; Hei, X.; Qiu, P.; Hu, X.; Luo, J.; He, X. Direction Discrimination Method for Small-Current Grounding Faults Based on XGBoost and Generalized Feature Optimization. *Electr. Power Autom. Equip.* **2025**, *45*, 71–79.
30. Miao, X.; Tang, L.; Zhuang, S.; Zhang, P. Review of Short-Circuit Fault Protection Methods in Low-Voltage Distribution Systems. *Electr. Energy Manag. Technol.* **2019**, *15*, 21–29.
31. Konuhova, M. Modeling of Induction Motor Direct Starting with and without Considering Current Displacement in Slot. *Appl. Sci.* **2024**, *14*, 9230. [CrossRef]